PHYSICAL REVIEW MATERIALS **5**, L063001 (2021)

Letter **Editors' Suggestion**

Inducing ferroelastic domains in single-crystal $CsPbBr_3$ perovskite nanowires using atomic force microscopy

Lucas A. B. Marçal,[1] Sandra Benter,[1] Austin Irish,[1] Dmitry Dzhigaev,[1] Eitan Oksenberg,[2,3] Amnon Rothman,[3] Ella Sanders,[3] Susanna Hammarberg,[1] Zhaojun Zhang,[1] Simone Sala,[4] Alexander Björling,[4] Eva Unger,[5,6] Anders Mikkelsen,[1] Ernesto Joselevich,[3] Rainer Timm,[1] and Jesper Wallentin[1,*]

[1]*Division of Synchrotron Radiation Research and NanoLund, Lund University, Box 118, 22100 Lund, Sweden*
[2]*Center for Nanophotonics, AMOLF, 1098 XG Amsterdam, Netherlands*
[3]*Department of Materials and Interfaces Weizmann Institute of Science, Rehovot 76100, Israel*
[4]*MAX IV Laboratory, Lund University, 22100 Lund, Sweden*
[5]*Helmholtz-Zentrum Berlin für Materialien und Energie GmbH, Young Investigator Group Hybrid Materials Formation and Scaling, Kekuléstraße 5, 12489 Berlin, Germany*
[6]*Division of Chemical Physics and NanoLund, Lund University, PO Box 124, 22100 Lund, Sweden*

(Received 2 February 2021; revised 29 March 2021; accepted 28 April 2021; published 1 June 2021)

Ferroelectric and ferroelastic domains have been predicted to enhance metal halide perovskite (MHP) solar cell performance. While the formation of such domains can be modified by temperature, pressure, or strain, established methods lack spatial control at the level of single domains. Here, we induce the formation of ferroelastic domains in $CsPbBr_3$ nanowires at room temperature using an atomic force microscope (AFM) tip and visualize the domains using nanofocused x-ray diffraction with a 60 nm beam. Regions scanned with a low AFM tip force show orthorhombic 004 reflections along the nanowire axis, while regions exposed to higher forces exhibit 220 reflections. The applied stress locally changes the crystal structure, leading to lattice tilts that define ferroelastic domains, which spread spatially and terminate at $\{112\}$-type domain walls. The ability to induce individual ferroelastic domains within MHPs using AFM gives new possibilities for device design and fundamental experimental studies.

DOI: 10.1103/PhysRevMaterials.5.L063001

I. INTRODUCTION

Metal halide perovskites (MHPs) have attracted great interest in the scientific community in the last years, mostly owing to their potential applications in next-generation solar cells, laser devices, and photodetectors [1–5]. MHP nanocrystals have additional degrees of freedom compared with their bulk counterparts and can show excellent brightness and narrow-band photoluminescence (PL) quantum yield [6–8]. Such advantages, together with the ability to tune the emission wavelength by varying their sizes, make nanowires of $CsPbBr_3$, a compound in this class that exhibits good radiation stability, especially promising for future optoelectronic applications [9,10]. Nanocrystals are also important model systems for understanding polycrystalline MHP thin film materials.

The crystal structure of MHPs affect their optical properties, which makes the ability to control the structure essential for technological applications [11–13]. The MHP studied here $CsPbBr_3$ crystallizes in an orthorhombic structure (*Pbnm* with $a = 8.20$ Å, $b = 8.25$ Å, and $c = 11.74$ Å, also commonly presented in the *Pnma* notation, with $a = 8.25$ Å, $b = 11.74$ Å, and $c = 8.20$ Å) at room temperature [14]. There is still debate regarding the ferroelectric nature of MHPs [15], but it is well known that they can show ferroelastic domains within the same crystal structure, which can affect their solar cell performance [15–17]. Theoretical reports have predicted that ferroelectricity could enhance carrier separation [16] and that ferroelastic domains could suppress nonradiative carrier recombination [17], in both cases enhancing the performance of MHP solar cells.

Controlling the formation of such domains could therefore be vital for fundamental studies as well as devices. Many reports have investigated the formation of ferroelectricity and ferroelasticity [18–21]. In ferroelectric materials, the application of an external electric field can switch the polarization of domains [22], while ferroelastic twins can be induced via temperature variation [19] or stress [20]. Gao *et al.* [21] used a diamond indenter to reversibly increase the size of a ferroelastic domain in a $Pb(Zr_{0.2}, Ti_{0.8})O_3$ thin film. In the case of MHPs, ferroelastic domain formation has so far been demonstrated by the application of external stress field [15,23] or heating [24], but these methods generally lack spatial control at the individual domain level.

Here, we use atomic force microscopy (AFM) [25,26] to locally induce ferroelastic domains within single-crystal

---

[*] jesper.wallentin@sljus.lu.se

$CsPbBr_3$ nanowires [27]. We use nanofocused x-ray diffraction (XRD) with 60 nm real space resolution to probe the altered lattice spacing and tilts in an extended crystal and show that AFM can locally create stable twins where the crystal orientation is changed from the orthorhombic (004) to (220), along the nanowire axis. The domains are formed and remain stable at room temperature. The ability to control the formation of ferroelastic domains in MHP single crystals can open possibilities for optoelectronic applications and experimental materials science [3,28].

II. EXPERIMENTAL

A. Growth

$CsPbBr_3$ nanowires were grown on a fused silica glass substrate by thermal evaporation at elevated temperatures >360 °C, analogous to previous reports [29–31]. Note that, for the experiment described here, nanowires were deposited on amorphous SiO_2 substrates instead of single-crystal sapphire [29] or mica [30,31]. The noncatalyzed growth was carried out in a three-zone horizontal-tube furnace. The quartz tube reactor was purged with a N_2 (99.999%, Gordon Gas) and H_2 (99.99995%, Parker Dominic Hunter H_2-generator) 7:1 mixture and maintained at 350 mbar with a constant 400 sccm flow of the N_2/H_2 mixture during the growth process. For the growth process, 150–180-μm-thick, ultraviolet-graded, fused silica glass (Laser Optex Inc.) substrates were used. CsBr and $PbBr_2$ powders (both purchased from Sigma-Aldrich) were mixed in a 1:2 molar ratio and heated at 390 °C for 20 min in the same N_2/H_2 atmosphere to generate the precursor. During the growth process, the precursor was held at 550 °C in the first heating zone of the furnace, while the silica glass samples were placed downstream in the second heating zone and held at 360 °C. After a 15 min growth period, the furnace was moved away, and the source and sample could be rapidly cooled down to room temperature.

B. Atomic force microscopy measurements

Some of the nanowires were locally manipulated using an AFM, as the AFM tip can apply high local forces and induce strain in a controlled way [32,33]. To characterize and manipulate the surface of the nanowires, two AFM setups were employed including the Nanowizard II from JPK and the Bruker dimension icon. For nanowire A, the Nanowizard was used in intermittent contact mode with highly *n*-doped Si cantilevers (PPP-NCHR from Nanosensors) with a nominal resonance frequency of 330 kHz and a force constant of 42 N/m. Piercing of the nanowire was accomplished by locally driving the cantilever into a ringing regime (i.e., a feedback loop with strong self-oscillation) while scanning the surface, resulting in the periodical pattern or even material removal at the corresponding positions. It should be noted that the scanning direction is tilted by 11 ° compared with the lower edge of the nanowire. By operating in TappingMode^{TM} and PeakForce QNM® at the Bruker AFM, the topology study and manipulation of nanowire B were performed. Therefore, a silicon nitride tip (ScanAsyst-Air from Bruker) with a nominal resonance frequency of 70 kHz was calibrated displaying a spring constant of 0.59 N/m and a deflection sensitivity of 70 nm/V. After attaining a complete overview of the wire, a 1.2 × 1.2 μm² area was scanned two times with a peak force setpoint of 40 nN and a peak force frequency of 2 kHz. The induced force during overview scans before and after in TappingMode was ∼1 nN.

C. Structural characterization

Nanofocused XRD was used to probe the crystal structure with high spatial resolution. XRD, known for being very sensitive to strain and lattice tilts, traditionally has poor spatial resolution, due to the limited x-ray beam focus size [34–37]. However, recent developments in x-ray optics, paired with increased photon flux from the new fourth-generation synchrotron x-ray sources [38], make it possible to focus x-ray beams down to the nanoscale, allowing the study of nanostructures with high real space resolution [24,39,40]. The XRD experiment was performed in transmission geometry using a nanofocused beam at the NanoMAX beamline, at MAX IV Laboratory in Lund, Sweden. The beam was focused to 63 × 61 nm² (vertical × horizontal) spot size using a set of KB mirrors. The energy of the beam was fixed at 14.000 keV (wavelength 0.8856 Å) during the nanodiffraction experiments, with an incident flux of 10^9 photons/s. The Bragg angle position was calibrated using a Si foil. The sample was mounted on a ThorLabs LCRM2 rotation mount, so that the nanowire could be rotated around the substrate surface normal. The sample holder with the rotation stage was attached to a fast *xyz* scanning piezoelectric stage, with a lateral stroke of 100 μm and a resolution of 10 nm. Gold markers on the sample allowed for a first alignment of the coarse motors using an in-line microscope. The diffracted beam was recorded using a Merlin photon-counting detector, with 515 × 515 pixels of 55 μm^2 pixel size positioned 400 mm away from the sample. A RaySpec single-element SDD, coupled with an XSPRESS3 pulse processor, was used to collect the x-ray fluorescence signal, which was used to verify the alignment of the nanowire during the scanning diffraction measurements. Real space misalignments of the nanowire were later compensated during data analysis. We simultaneously combined high-speed continuous motion of the *xyz* scanning piezoelectric stage and high-frequency data acquisition, as a function of the real space position along the nanowire. The data were then used to obtain two-dimensional diffraction maps and then reconstruct real space maps of the sample for different Bragg angles.

A schematic representation of the experimental setup can be seen in Fig. 1. We obtained real space maps of the nanowire, by positioning a two-dimensional x-ray detector at the 2θ Bragg condition of the 004 reflection of the $CsPbBr_3$ orthorhombic (*Pbnm*) phase and scanning the sample with a nanofocused beam. To obtain spatially resolved lattice spacing and tilt maps, we scanned the sample at different θ values around the Bragg condition, i.e., a rocking curve, and evaluated the three-dimensional reciprocal space [39,41]. The definition of the real and reciprocal space coordinates, as well as lattice tilts, can be seen in the inset of Fig. 1. The nanowire axis was set along z, so the 004 Bragg reflection main scattering component is q_z. The lattice tilts α, β, and γ are defined as the lattice rotations around q_y, q_x, and q_z, respectively. The

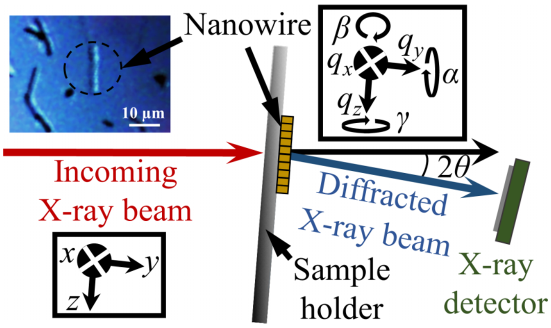

FIG. 1. Schematic representation of the nanofocused scanning x-ray diffraction (XRD) experimental setup. The nanowire was rotated to the Bragg angle θ, and the x-ray detector was positioned at 2θ. The scattering vector components q_x, q_y, and q_z, as well as lattice tilts α (rotation around q_y), β (rotation around q_x), and γ (rotation around q_z) are defined in the inset. The nanowire axis was set along z and the sample normal along y, so that q_z is the main scattering component of the 004 Bragg reflection. The coordinate system rotates as the nanowire is rotated around the sample normal (q_y axis).

coordinate system was rotated with the nanowire when it was rotated around the sample normal, as discussed below.

We investigated multiple single-crystal nanowires, both pristine and manipulated by AFM, of which two of the manipulated nanowires are presented in the main text. Pristine nanowires, as exemplified in Fig. S1 in the Supplemental Material [42], generally show a single 004 Bragg peak throughout the crystal [24], related to crystal planes with an average lattice spacing of 2.945 ± 0.004 Å. The nanowires only show small variations in lattice spacing (strain), except at the ends which typically show a slightly smaller (0.5%) lattice spacing, but with a local variation in lattice tilt of a few tenths of a degree.

III. RESULTS

A. Nanowire A: Severe damage through strong AFM tip interaction

Nanowire A (17.5 μm long, 1.1 μm wide, and 81 nm thick) was impacted by the AFM tip in two different regions. For this purpose, the AFM cantilever was excited into a hard tapping regime during individual scanlines. An AFM image of nanowire A, measured after manipulation, can be seen in Fig. 2(a). Slightly to the right of the center, some material was removed, leaving a triangular-shaped hole in the structure. Further damage was induced on the left-hand third of the nanowire, where high local pressure from the AFM tip pierced the structure while scanning in ringing regime. This caused an indentation pattern with periodicity of ~350 nm. The direction of both the indentation and the hole correspond to the scan direction of the AFM tip.

The AFM manipulation led to structural changes, which are more unexpected than the removal of material from the relatively soft $CsPbBr_3$ nanowire. The sum of the diffraction frames acquired along the nanowire A can be seen in Fig. 2(b), showing multiple peaks, unlike the single 004 peak observed in pristine nanowires. In this geometry, the main scattering vector component q_z is oriented horizontally, meaning that strain or different lattice plane spacings in this direction will lead to variations and splits in the horizontal direction. Variations in the vertical direction are instead due to different lattice orientations, tilts. The Bragg peaks spread along two different Debye-Scherrer rings, corresponding to different lattice spacings (d spacing), which indicates significant changes in the crystal structure. Note, however, the lack of diffraction in between the two Debye-Scherrer rings that correspond to two distinct lattice spacings. The square shape of the Bragg peaks comes from the aperture of the focusing mirrors. We calculated the lattice spacing as a function of

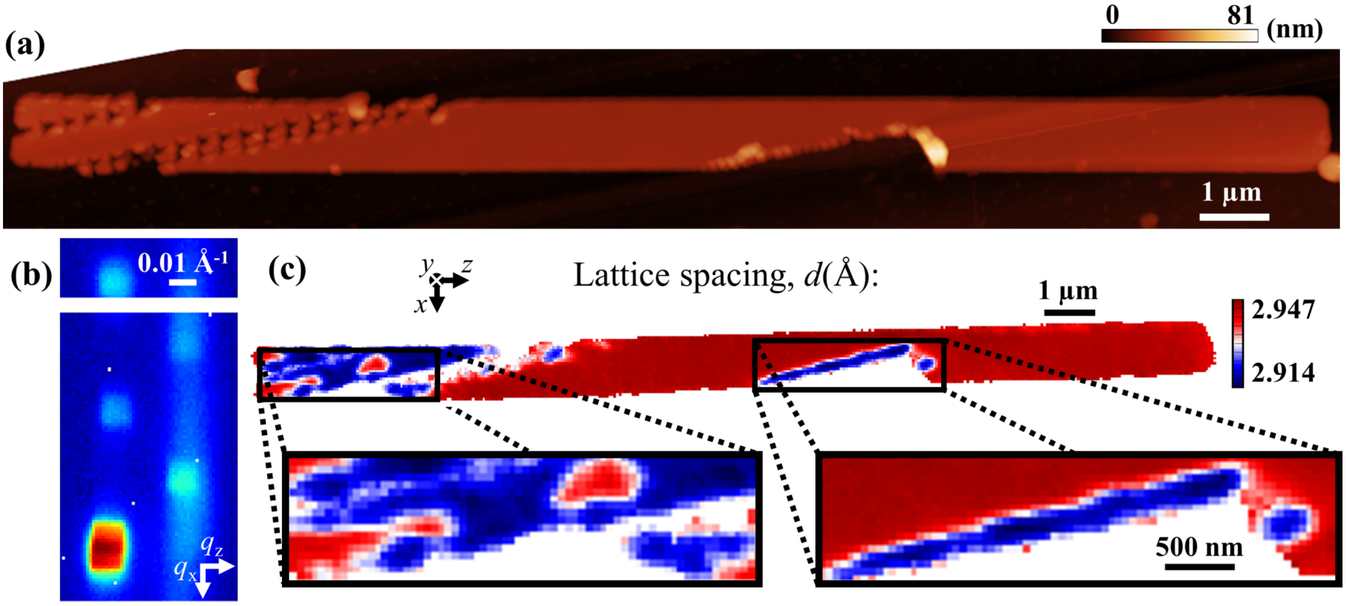

FIG. 2. (a) Atomic force microscopy (AFM) image of nanowire A after manipulation. (b) Sum of the diffraction frames acquired after AFM manipulation, evidencing the presence of multiple Bragg peaks. The white stripe is a detector module gap. (c) Map of the d spacing in the lattice. Insets show higher resolution images near the manipulated regions.

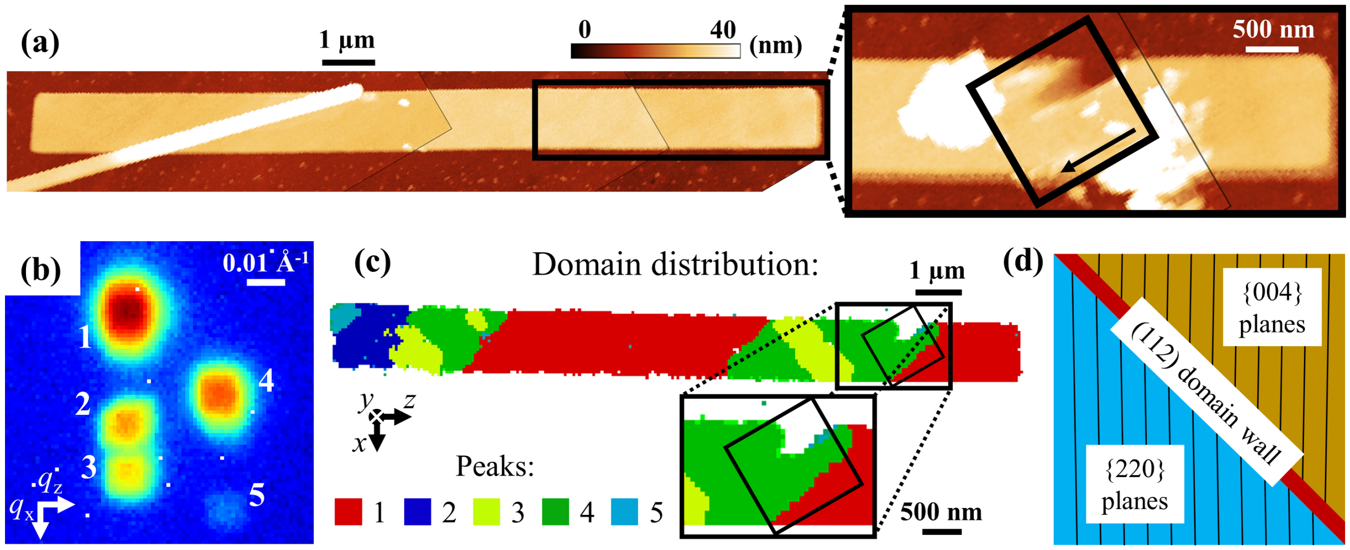

FIG. 3. (a) Atomic force microscopy (AFM) image of nanowire B before manipulation. Another nanowire can be seen crossing its left part. The image is stitched together from three AFM images. The inset shows a zoom of the right part of nanowire B, acquired after manipulation and evidencing the damaged region, represented by the black square. The arrow indicates the AFM scan direction, which is angled 30° relative to the nanowire long axis. (b) Sum of the x-ray diffraction after manipulation, evidencing the presence of multiple Bragg peaks. (c) Map plotting the real space distribution of domains associated with the different peaks, numbered from 1 to 5, as marked in (b). The inset shows a more detailed view near the peak force scan area, same as in (a), marked with the black box. (d) Schematic model of domains orientation near a {112}-type domain wall. Straight lines represent the atomic planes. Note slight differences in line spacing and rotation representing the variations in d spacing and lattice tilt for neighboring domains.

position, creating a map as shown in Fig. 2(c). Magnified plots of both manipulated regions, evidencing abrupt variations in the plane spacing, are also plotted. Importantly, we find that the lattice spacing only changed near the most strongly manipulated regions. In these areas, the d spacing was on average 2.924 ± 0.004 Å. In the other regions, which were imaged in AFM tapping mode, we observe an average d spacing of 2.943 ± 0.004 Å, like the pristine reference nanowire, with only small variations. A more detailed analysis of the crystal structure of nanowire A can be found in Fig. S2 in the Supplemental Material [42].

B. Nanowire B: Moderate manipulation through controlled force application

Nanowire B (15 μm long, 1.2 μm wide, and 40 nm in thick) was gently manipulated by AFM to avoid material removal and more thoroughly investigated by XRD. Initially, the entire nanowire was carefully imaged by AFM in tapping mode, with a force of ~1 nN applied locally to the nanowire surface. Subsequently, a small region near the right end was more strongly manipulated by two area scans in the same area ($1.2 \times 1.2\,\mu\text{m}^2$) in peak force mode, using the same AFM tip and a peak force setpoint of 40 nN. Figure 3(a) shows the AFM image obtained before manipulation. Note the presence of another nanowire crossing the left part of nanowire B (crossing region). The inset plots the area marked in Fig. 3(a) after damage by the AFM tip, evidencing the affected region. The black box represents the peak force scan area, and the arrow indicates the scan direction.

After AFM manipulation, we performed scanning XRD as described above. We observed five different discrete Bragg peaks, with two different d spacings, originating in different regions of the nanowire. In Fig. 3(b), we show the sum of the diffraction frames, with the Bragg peaks indexed from 1 to 5. The presence of two Debye-Scherrer rings and the discrete distribution of the Bragg peaks along the two rings is an indication that the domains in the nanowire present distinct orientations and not a gradual variation. A map showing the real space domains associated with each peak, plotted in Fig. 3(c), correlates reciprocal and real space. Well-defined color contrast regions indicate that domains with different crystal structures or orientations interface each other along diagonal domain walls. Note that the domain walls seen in Fig. 3(c), angled ~45° relative to the nanowire axis, do not match the AFM scanning direction, at 30°. One possibility is that the two Debye-Scherrer rings correspond to the orthorhombic 004 and 220 reflections and that the domain walls are oriented parallel to the {112}-type planes. A schematic model representing this possibility is shown in Fig. 3(d), where two subsequent domains with (004) and (220) planes oriented along the nanowire axis depicted in yellow and blue, respectively, while the (112) domain wall is marked in red.

Although the XRD results so far clearly demonstrate structural changes, it is not sufficient to accurately determine the nature of these changes. In XRD, only crystal planes orthogonal to the scattering vector **Q** will be detected. Therefore, nanofocused scanning XRD measurements of nanowire B were performed in three different geometries: with the scattering vector parallel, orthogonal, and diagonal (45° angle) with the nanowire axis. Five Bragg peaks were observed, specified with the subscript P or O, in the parallel and orthogonal nanowire orientations, as seen in Figs. 4(a) and 4(b). Figures 4(c) and 4(d) show maps of the d spacing (upper

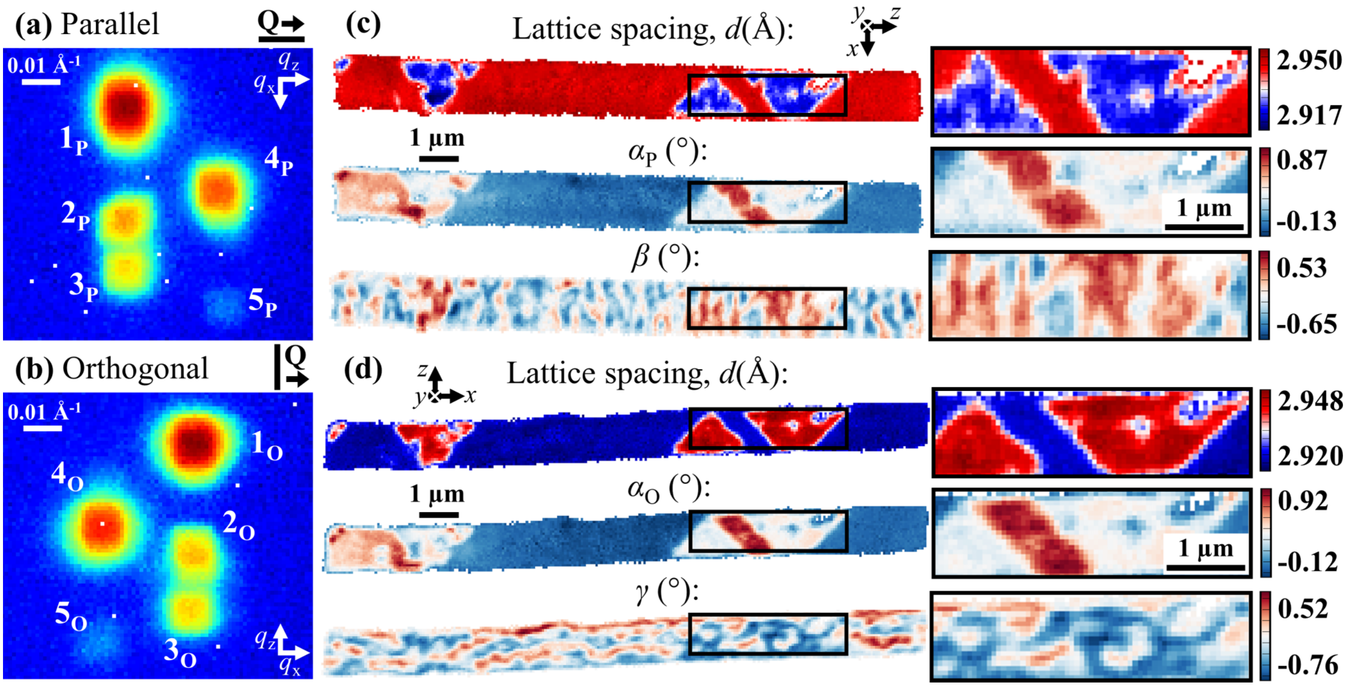

FIG. 4. (a) and (b) Sum of the diffraction frames acquired with the scattering vector **Q** parallel and orthogonal to the nanowire axis, respectively. Peaks are indexed from 1 to 5, followed by letters P and O, indicating parallel and orthogonal geometries, respectively. (c) Maps plotting the d spacing and the α and β tilts, with **Q** parallel to the nanowire axis. (d) Maps plotting the d spacing and the α and γ tilts, with **Q** orthogonal to the nanowire axis. Insets show magnified plots from the marked areas in (c) and (d). Note that the map in (d) is shown rotated to the same orientation as (c) to make comparisons easier, although the acquisition was done with the nanowire rotated orthogonal to the **Q** vector. The indicated coordinate vectors show the actual nanowire orientation in each geometry, always with the axis along z.

panel), the α tilt around the sample normal q_y axis (middle panel), and the tilt around the in-plane axes β and γ (bottom panel) retrieved from the parallel and orthogonal geometries, respectively. Note that, in the latter case, the tilt γ is plotted instead of β, which is not visible in this geometry. Although measurements were done by rotating the nanowire around the sample surface normal, all images are shown here with the nanowire in the same orientation to help the comparison in real space. The coordinate vectors in Figs. 4(c) and 4(d) evidence the actual nanowire orientation in each geometry, as its axis is always set along z, even if it is rotated around the sample normal. In the diagonal geometry, three peaks, all along the same Debye-Scherrer ring, could be seen. These are indexed as peaks 6–8 and are shown in Fig. 5(a). The domain distribution retrieved from the parallel, orthogonal, and diagonal geometries are plotted in Figs. 5(b)–5(d), respectively. Again, all the nanowire plots were set horizontally for better comparison, while the coordinate vectors show the actual orientation in each geometry. The maps show that peaks 1_P and 1_O correspond to the same domains. The same is true for peaks $2_P/2_O$, $3_P/3_O$, $4_P/4_O$, and $5_P/5_O$. A complete analysis of the lattice spacing and tilts for both parallel and orthogonal geometries can be found in Fig. S3 in the Supplemental Material [42]. Real space maps reconstructed from the diagonal geometry are presented in Fig. S4 in the Supplemental Material [42]. We observe an overall tensile strain of $\sim 0.3\%$ compared with the bulk $CsPbBr_3$ lattice parameters [14], which is assigned to residual stress from the high temperature growth [43,44].

C. Crystal structure analysis

The comprehensive measurements of nanowire B make it possible to understand the nature of these local changes. First, we note that peaks 1_P, 2_P, and 3_P show an average d spacing of 2.944 ± 0.004 Å, very similar to the pristine reference nanowire as well as the nonmanipulated areas of nanowire A. In contrast, peaks 4_P and 5_P are observed at a larger q_z, i.e., a smaller d spacing of 2.927 ± 0.004 Å. In the orthogonal geometry, we find the opposite result, that 1_O, 2_O, and 3_O show a d spacing of 2.926 ± 0.004 Å, while 4_O and 5_O show d spacing of 2.942 ± 0.004 Å. The average measured distance between these two sets of peaks, i.e., the two Debye-Scherrer rings, is in both cases 0.022 ± 0.002 Å^{-1}, like the theoretical 0.020 ± 0.001 Å^{-1} difference between the scattering vectors of orthorhombic 004 and 220 Bragg reflections [14].

The results show that domains present orthorhombic crystal structure with the unit cells rotated by 90° around q_y. Peaks 1_P, 2_P, and 3_P correspond to the orthorhombic 004, while peaks 4_P and 5_P result from the orthorhombic 220 Bragg reflections. The opposite is true in the orthogonal geometry, where peaks 1_O, 2_O, and 3_O correspond to orthorhombic 220 and peaks 4_O and 5_O to orthorhombic 004 reflections. These observations are consistent since the (220) and (004) planes are orthogonal, i.e., a domain showing a 004 reflection in the parallel geometry shows a 220 reflection in the orthogonal geometry and vice versa. It means that q_x and q_y are $[1\bar{1}0]$ and [110], respectively, in the untreated regions. This also means that the peaks 6–8 observed in the diagonal geometry correspond to orthorhombic 112 reflections. In this geometry,

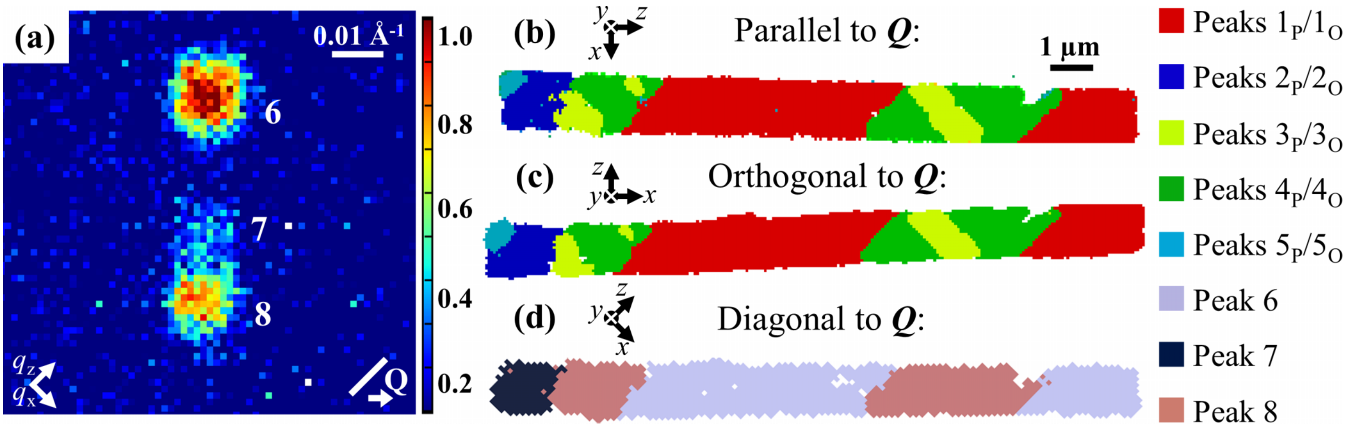

FIG. 5. (a) Sum of the diffraction frames acquired from nanowire B when the **Q** vector was oriented diagonal to the nanowire axis. (b)–(d) Maps plotting the real space distribution of domains associated to different peaks, retrieved with the nanowire aligned (b) parallel, (c) orthogonal, and (d) diagonal to the **Q** vector. Maps in (b)–(d) were set in the same orientation for better comparison, while the coordinate vectors evidence the actual nanowire orientation in each geometry, always with the axis along z.

all domains will diffract along the same Debye-Scherrer rings, leading to superpositions of 112 and $\bar{1}\bar{1}2$ peaks and therefore fewer peaks on the detector. Thus, the results confirm our initial hypothesis.

D. AFM and XRD correlation

It is important to notice how the local manipulation through the AFM tip correlates with the observed structural changes. A major part of the area manipulated by AFM with higher peak force has undergone a structural change, as can be seen from Figs. 3(a) and 3(c), resulting in the peak 4 reflection. However, the structural changes are not restricted to the 1.2 × 1.2 μm area that was directly affected by the AFM tip but instead extends for about 4 μm and consists of tilted domains. This indicates that the peak force of 40 nN applied by the AFM tip has initiated the structural changes, but their spatial extension is determined by an internal domain structure of the nanowire rather than the direct interplay with the AFM tip.

Figures 3(a) and 3(c) further show that nanowire material is missing in a small fraction of the area that had been manipulated by the AFM tip toward the edge of the nanowire. It must be noted that the movement of the AFM tip during manipulation of the nanowire was from top right to bottom left, starting the individual scan lines slightly outside the nanowire region, then moving up the steep side facet of the nanowire and continuing on the top facet. This scan movement involves significant lateral forces toward the site facet of the nanowire [45], which probably are responsible for the local removal of nanowire material. Crystal changes also appeared in the left part of the nanowire in Fig. 3(c), in an area that was only imaged in AFM light tapping mode, which comes along with relatively small forces when scanning flat surfaces (here ~1 nN). However, this position is in close proximity to another crossing nanowire, as seen in Fig. 3(a), and moving the tip across the steep site faces of this crossing nanowire can again apply relatively strong forces, both on the small crossing nanowire but also on the material of the larger nanowire lying underneath. These forces are most probably responsible for the observed structural change.

Naturally, it is interesting to attempt to quantify the local stress and strain involved. In a simplified theoretical approach, considering no plastic deformation, we estimate the elastic strain in nanowire B as induced by the AFM tip. The force applied by the tip in each direction will put a certain stress locally on the nanowire, inducing local strain according to Young's modulus of the nanowire material. The peak force setpoint was chosen as $F = 40\,\text{nN}$ during AFM manipulation of nanowire B. In a simplified approximation, this force is applied on an area $A = \pi \times R^2$, with a tip radius of about $R = 10\,\text{nm}$, resulting in a local stress $\sigma = F/A = 0.13\,\text{GPa}$. Note that the actual contact area is slightly larger than the cross-section of the tip and depends on the applied force as well as Young's modulus and the Poisson ratio of both tip and sample material. Young's modulus Y of bulk CsPbBr_3 was reported in the literature to be on the order of 20 GPa [46]. Thus, in the elastic regime, the stress induced by the AFM tip would result in local strain ε according to $\varepsilon = \sigma/Y = 0.6\%$. This rough estimation of AFM-induced strain agrees very well with the nano-XRD results, which show internal strain variation on the order of 1% or less, when comparing domains with different crystallographic orientation. The calculations here were based on a static model, but in reality, the AFM tip moves dynamically across the surface, which could lead to higher forces. Indeed, the structural changes observed on the left part of nanowire B (crossing region) suggest AFM tip dynamic movement, which could significantly impact the stress analysis. Furthermore, the AFM-induced stress can vary significantly at the atomic level, e.g., at surface steps and especially when scanning across the edge of the nanowire. Indeed, the latter behavior has resulted in local material removal, i.e., plastic deformation, at the edge of nanowire B, as seen in the inset of Fig. 3(a). Nevertheless, we believe that a future study of the stress-strain relation, both for refinement of the Young's modulus for CsPbBr_3 nanostructures as well as testing the limits for elastic deformation of the nanowires, would be possible but requires a controlled and systematic approach for applying different stress on several nanowires using the AFM tip.

E. Domain walls and lattice tilts

The lattice spacing maps also reveal distinct shapes of the domains, with interfaces oriented 45 ° relative to the nanowire edges. It is known from the literature that ferroelastic materials can form domain walls along crystallographic planes, and the (112) plane is a permissible domain wall for different MHPs [47,48]. The observation of {112} twin planes have been recently reported for $CsPbBr_3$ films by Zhang *et al.* [49], and here, we observe the same {112} domain walls enclosing ferroelastic domains in an extended nanostructure.

XRD is highly sensitive to local variations in lattice tilt, which can be used to analyze ferroelastic domains. Both parallel and orthogonal geometries present similar α maps, with lattice tilt variations on the order of 1 °. This tilt corresponds to a rotation around the optical axis and results in the peak splitting along the Debye-Scherrer rings, i.e., the splitting of 1, 2, and 3 from each other. A bending of the nanowire would be seen as a continuous increase in the local tilt, leading to a smearing of the integrated Bragg peak along the Debye-Scherrer ring [50]. This is locally observed here within domains in Fig. S3 in the Supplemental Material [42]. In contrast, abrupt α tilt changes of ∼0.32 ° are observed between neighboring domains, and indeed this is the reason we observe multiple discrete peaks rather than rings. The β and γ maps also present similarities in both geometries, with an undulation profile exhibiting maximum and minimum values with 1 ° variation in ∼300 nm. The difference, in this case, is that the wave is along the nanowire axis for β and perpendicular for γ.

The stepwise variation in the lattice tilt α is due to the change in the crystal structure, which aligns orthorhombic unit cells with the c axis along orthogonal directions. The crystal responds to the lattice mismatch at the domain walls with a lattice tilt, which is like well-known *a*/*c*/*a*-type domains described for different ferroelastic materials [51]. For the parallel geometry, on average, the peak 1 and 4 domains present d spacings of 2.944 and 2.927 Å, respectively. In the orthogonal geometry, these values change to 2.926 and 2.942 Å. Such findings point to average mismatches of $2.944-2.927 = 0.017$ Å and $2.942-2.926 = 0.016$ Å along and orthogonal to the nanowire axis, respectively. This would lead to lattice tilts of $\omega = 1-[(a^2+b^2)^{1/2}/c] = 1-(2.927/2.944) = 0.33 \pm 0.11^\circ$ and $\omega = 1-(2.926/2.942) = 0.31 \pm 0.11^\circ$ around q_y. The measured average tilts on domains 1–5 are 0.01 °, 0.46 °, 0.67 °, 0.35 °, and 0.84 °, respectively. It is notable that α variation between domains 1 and 4, which interface each other, is 0.34 ° and between domains 3 and 4 it is 0.32 °, in excellent agreement with the calculated value.

IV. CONCLUSIONS

In conclusion, we have shown that AFM can be used to locally create ferroelastic domains within single-crystal $CsPbBr_3$ nanowires. More specifically, scanning nano-XRD shows that (110)-oriented domains are created within the nanowire that otherwise has the (001) planes orthogonal to the long axis. While the domains only appear near strongly manipulated areas, they can extend slightly beyond this region and terminate at {112}-type domain walls. The observed lattice tilts are in excellent agreement with calculations based on the lattice mismatches. The ability to induce individual ferroelastic domains within MHPs using a standard AFM opens possibilities for device design and fundamental experimental studies. The method presented here should be applicable to a wide range of materials, including other types of perovskites.

ACKNOWLEDGMENTS

This project has received funding from the European Research Council (ERC) under the European Union's Horizon 2020 Research and Innovation Programme (Grant No. 801847). This research was also funded by the Olle Engkvist Foundation, NanoLund, and Marie Sklodowska Curie Actions Cofund, Project INCA 600398. We acknowledge MAX IV Laboratory for time on Beamline NanoMAX under Proposal 20190248. Research conducted at MAX IV, a Swedish national user facility, is supported by the Swedish Research Council under Contract No. 2018-07152, the Swedish Governmental Agency for Innovation Systems under Contract No. 2018-04969, and Formas under Contract No. 2019-02496. E.J. acknowledges support from the ERC PoC Grant (No. 838702) and the Israel Science Foundation (No. 2444/19). E.J. holds the Drake Family Professorial Chair of Nanotechnology.

L.A.B.M. and J.W. planned the research and wrote the paper. Sample synthesis was performed by E.O., A.R., E.S., and E.J. AFM measurements were performed by S.B., A.I., and R.T. Nanofocused scanning XRD measurements were performed by L.A.B.M., D.D., S.H., Z.Z., S.S., A.B., and J.W. Data analysis was performed by L.A.B.M. and J.W. All authors discussed the data and contributed to the paper.

The authors declare no competing financial interest.

---

[1] W. Zhang, G. E. Eperon, and H. J. Snaith, Nature Energy **1**, 16048 (2016).

[2] T. A. S. Doherty *et al.*, Nature **580**, 360 (2020).

[3] A. Dobrovolsky, A. Merdasa, E. L. Unger, A. Yartsev, and I. G. Scheblykin, Nat Commun. **8**, 34 (2017).

[4] A. Amat, E. Mosconi, E. Ronca, C. Quarti, P. Umari, M. K. Nazeeruddin, M. Gratzel, and F. De Angelis, Nano Lett. **14**, 3608 (2014).

[5] E. Oksenberg, E. Sanders, R. Popovitz-Biro, L. Houben, and E. Joselevich, Nano Lett. **18**, 424 (2018).

[6] M. V. Kovalenko, L. Protesescu, and M. I. Bodnarchuk, Science **358**, 745 (2017).

[7] M. S. Kirschner, B. T. Diroll, P. Guo, S. M. Harvey, W. Helweh, N. C. Flanders, A. Brumberg, N. E. Watkins, A. A. Leonard, A. M. Evans, M. R. Wasielewski, W. R. Dichtel, X. Zhang, L. X. Chen, and R. D. Schaller, Nat Commun. **10**, 504 (2019).

[8] S. Park, H. Cho, W. Choi, H. Zou, and D. Y. Jeon, Nanoscale Adv. **1**, 2828 (2019).

[9] A. P. Schlaus, M. S. Spencer, K. Miyata, F. Liu, X. Wang, I. Datta, M. Lipson, A. Pan, and X. Y. Zhu, Nat. Commun. **10**, 265 (2019).

[10] Y. Liu, M. Guo, S. Dong, X. Jiao, T. Wang, and D. Chen, J. Mater. Chem. C **6**, 7797 (2018).

[11] Y. Nagaoka, K. Hills-Kimball, R. Tan, R. Li, Z. Wang, and O. Chen, Adv. Mater. **29**, 1606666 (2017).

[12] S. Yesudhas, M. V. Morrell, M. J. Anderson, C. A. Ullrich, C. Kenney-Benson, Y. Xing, and S. Guha, Chem. Mater. **32**, 785 (2019).

[13] L. Zhang, Q. Zeng, and K. Wang, J. Phys. Chem. Lett. **8**, 3752 (2017).

[14] C. C. Stoumpos, C. D. Malliakas, J. A. Peters, Z. Liu, M. Sebastian, J. Im, T. C. Chasapis, A. C. Wibowo, D. Y. Chung, A. J. Freeman, B. W. Wessels, and M. G. Kanatzidis, Cryst. Growth Des. **13**, 2722 (2013).

[15] E. Strelcov, Q. Dong, T. Li, J. Chae, Y. Shao, Y. Deng, A. Gruverman, J. Huang, and A. Centrone, Sci. Adv. **3**, e1602165 (2017).

[16] J. M. Frost, K. T. Butler, F. Brivio, C. H. Hendon, M. van Schilfgaarde, and A. Walsh, Nano Lett. **14**, 2584 (2014).

[17] R. Shi, Z. Zhang, W. H. Fang, and R. Long, Nanoscale Horiz **5**, 683 (2020).

[18] H. H. Huang, Z. Hong, H. L. Xin, D. Su, L. Q. Chen, G. Huang, P. R. Munroe, and N. Valanoor, ACS Nano **10**, 10126 (2016).

[19] R. J. Harrison, S. A. T. Redfern, and E. K. H. Salje, Phys. Rev. B **69**, 144101 (2004).

[20] S. Choudhury, J. X. Zhang, Y. L. Li, L. Q. Chen, Q. X. Jia, and S. V. Kalinin, Appl. Phys. Lett. **93**, 162901 (2008).

[21] P. Gao, J. Britson, C. T. Nelson, J. R. Jokisaari, C. Duan, M. Trassin, S. H. Baek, H. Guo, L. Li, Y. Wang, Y. H. Chu, A. M. Minor, C. B. Eom, R. Ramesh, L. Q. Chen, and X. Pan, Nat. Commun. **5**, 3801 (2014).

[22] W. J. Merz, Phys. Rev. **95**, 690 (1954).

[23] X. Xiao, W. Li, Y. Fang, Y. Liu, Y. Shao, S. Yang, J. Zhao, X. Dai, R. Zia, and J. Huang, Nat. Commun. **11**, 2215 (2020).

[24] L. A. B. Marcal, E. Oksenberg, D. Dzhigaev, S. Hammarberg, A. Rothman, A. Bjorling, E. Unger, A. Mikkelsen, E. Joselevich, and J. Wallentin, ACS Nano **14**, 15973 (2020).

[25] S. Yngman, F. Lenrick, Y.-P. Liu, Z. Ren, M. Khalilian, B. J. Ohlsson, D. Hessman, L. Samuelson, R. Timm, and A. Mikkelsen, Rev. Sci. Instrum. **90**, 103703 (2019).

[26] J. Song, Y. Zhou, N. P. Padture, and B. D. Huey, Nat. Commun. **11**, 3308 (2020).

[27] Y. Tian, A. Merdasa, E. Unger, M. Abdellah, K. Zheng, S. McKibbin, A. Mikkelsen, T. Pullerits, A. Yartsev, V. Sundstrom, and I. G. Scheblykin, J. Phys. Chem. Lett. **6**, 4171 (2015).

[28] S. Neutzner, A. R. Srimath Kandada, G. Lanzani, and A. Petrozza, J. Mater. Chem. C **4**, 4630 (2016).

[29] E. Oksenberg, A. Merdasa, L. Houben, I. Kaplan-Ashiri, A. Rothman, I. G. Scheblykin, E. L. Unger, and E. Joselevich, Nat. Commun. **11**, 489 (2020).

[30] Y. Wang, X. Sun, R. Shivanna, Y. Yang, Z. Chen, Y. Guo, G. C. Wang, E. Wertz, F. Deschler, Z. Cai, H. Zhou, T. M. Lu, and J. Shi, Nano Lett. **16**, 7974 (2016).

[31] J. Chen, Y. Fu, L. Samad, L. Dang, Y. Zhao, S. Shen, L. Guo, and S. Jin, Nano Lett. **17**, 460 (2017).

[32] Z. Ren, F. Mastropietro, A. Davydok, S. Langlais, M. I. Richard, J. J. Furter, O. Thomas, M. Dupraz, M. Verdier, G. Beutier, P. Boesecke, and T. W. Cornelius, J. Synchrotron Radiat. **21**, 1128 (2014).

[33] Z. Zhao, X. Pu, C. Han, C. Du, L. Li, C. Jiang, W. Hu, and Z. L. Wang, ACS Nano **9**, 8578 (2015).

[34] S. O. Hruszkewycz, Q. Zhang, M. V. Holt, M. J. Highland, P. G. Evans, and P. H. Fuoss, Phys. Rev. A **94**, 043803 (2016).

[35] S. O. Hruszkewycz, M. J. Highland, M. V. Holt, D. Kim, C. M. Folkman, C. Thompson, A. Tripathi, G. B. Stephenson, S. Hong, and P. H. Fuoss, Phys. Rev. Lett. **110**, 177601 (2013).

[36] F. Bertolotti, G. Nedelcu, A. Vivani, A. Cervellino, N. Masciocchi, A. Guagliardi, and M. V. Kovalenko, ACS Nano **13**, 14294 (2019).

[37] F. Bertolotti, L. Protesescu, M. V. Kovalenko, S. Yakunin, A. Cervellino, S. J. L. Billinge, M. W. Terban, J. S. Pedersen, N. Masciocchi, and A. Guagliardi, ACS Nano **11**, 3819 (2017).

[38] A. Bjorling, S. Kalbfleisch, M. Kahnt, S. Sala, K. Parfeniukas, U. Vogt, G. Carbone, and U. Johansson, Opt. Express **28**, 5069 (2020).

[39] J. Wallentin, D. Jacobsson, M. Osterhoff, M. T. Borgstrom, and T. Salditt, Nano Lett. **17**, 4143 (2017).

[40] L. Chayanun, S. Hammarberg, H. Dierks, G. Otnes, A. Bjorling, M. T. Borgstrom, and J. Wallentin, Crystals **9**, 432 (2019).

[41] L. A. B. Marçal, M. I. Richard, R. Magalhães-Paniago, F. Cavallo, M. G. Lagally, O. G. Schmidt, T. Ü. Schülli, C. Deneke, and A. Malachias, Appl. Phys. Lett. **106**, 151905 (2015).

[42] See Supplemental Material at http://link.aps.org/supplemental/10.1103/PhysRevMaterials.5.L063001 for the pristine nanowire and detailed maps of nanowire A.

[43] R. B. Hetnarski, *Encyclopedia of Thermal Stresses* (Springer Netherlands, Dordrecht, 2014).

[44] G. Abadias, E. Chason, J. Keckes, M. Sebastiani, G. B. Thompson, E. Barthel, G. L. Doll, C. E. Murray, C. H. Stoessel, and L. Martinu, J. Vac. Sci. Tech. **36**, 020801 (2018).

[45] J. L. Webb, O. Persson, K. A. Dick, C. Thelander, R. Timm, and A. Mikkelsen, Nano Res. **7**, 877 (2014).

[46] X. Li, Y. Meng, R. Fan, S. Fan, C. Dang, X. Feng, J. C. Ho, and Y. Lu, Nano Res. (2021), doi: 10.1007/s12274-021-3332-0.

[47] H. T. Jeong, Y. C. Cho, C. R. Cho, and S.-Y. Jeong, J. Phys. Soc. Japan **70**, 717 (2001).

[48] J. Sapriel, Phys. Rev. B **12**, 5128 (1975).

[49] X. Zhang, F. Wang, B.-B. Zhang, G. Zha, and W. Jie, Cryst. Growth Des. **20**, 4585 (2020).

[50] J. Wallentin, M. Osterhoff, and T. Salditt, Adv. Mater. **28**, 1788 (2016).

[51] J. S. Speck, A. C. Daykin, A. Seifert, A. E. Romanov, and W. Pompe, J. Appl. Phys. **78**, 1696 (1995).